Title: Preparation of high surface area activated carbon from waste-biomass of sunflower piths: Kinetics and equilibrium studies on the dye removal

Authors: Mustafa Baysal, Kaan Bilge, Bengisu Yılmaz, Melih Papila, Yuda Y*ürü*m

PII: S2213-3437(18)30092-7
DOI: https://doi.org/10.1016/j.jece.2018.02.020
Reference: JECE 2212

To appear in:

Received date: 5-10-2017
Revised date: 15-1-2018
Accepted date: 12-2-2018

Please cite this article as: Mustafa Baysal, Kaan Bilge, Bengisu Yılmaz, Melih Papila, Yuda Y*ürü*m, Preparation of high surface area activated carbon from waste-biomass of sunflower piths: Kinetics and equilibrium studies on the dye removal, Journal of Environmental Chemical Engineering https://doi.org/10.1016/j.jece.2018.02.020

Preparation of high surface area activated carbon from waste-biomass of sunflower piths: Kinetics and equilibrium studies on the dye removal

Mustafa Baysal[1], Kaan Bilge[1], Bengisu Yılmaz[1], Melih Papila[1], Yuda Yürüm[1]*

[1]Sabancı University, Faculty of Engineering and Natural Sciences, Materials Science and NanoEngineering Program, Istanbul, Turkey
*Corresponding author: kaanbilge@sabanciuniv.edu

Highlights

- Use of waste sunflower pith as a precursor for activated carbon for the first time.
- High surface area AC prepared by NaOH and KOH (2690 $m^2 g^{-1}$ and 2090 $m^2 g^{-1}$).
- Microstructure of the SP in its natural form are shown by micro-computed tomography.
- Carbonization leads to SP into thin, separated carbon flakes of 200 nm thickness.
- Meso and micropores in the N-SPAC lead to a high MB adsorption (965.349 mg/g)

Abstract

Sunflower pith (SP), a vast agricultural waste is herein used as a precursor material for highly porous low density activated carbon production. Porosity and flake-like microstructure of the SP in its natural form are shown by micro-computed tomography (Micro-CT). Carbonization process turns the SP into thin, separated carbon flakes of 200 nm thickness. Two types of alkaline based chemical activation with KOH and NaOH are performed to yield SP based activated carbon (AC), K-SPAC and N-SPAC, respectively. Microstructural changes upon carbonization and activation process are elaborated by RAMAN, FTIR and SEM analyses. BET Surface area of the NaOH-activated N-SPAC was calculated as 2690 m^2/g and was higher than KOH-activated K-SPAC with 2090 m^2/g. Maximum adsorption capacity of N-SPAC was calculated as 965mg/g whereas it was 580 mg/g for K-SPAC. Adsorption kinetic studies for N-SPAC revealed that at a low initial concentration of dye (500 mg/L), the pseudo first-order kinetic model was predictive. On the other hand, at high initial MB concentration (1000 mg/L), the results indicate that the adsorption kinetics follow the Elovich model with intraparticle diffusion as one of the rate-determining steps.
In conclusion, overall results suggest that thanks to its highly porous microstructure, the SP is an alternative renewable AC precursor choice for dye removal applications.

Keywords: Sunflower pith, Char, Activated Carbon, CTscan, Adsorption

1. Introduction

Activated carbons (ACs) are highly porous materials with the inherent high surface area and high adsorption capacity [1]. Due to their adsorptive properties, ACs are commonly employed in purification and discolorization efforts that aim to decrease the concentration of environmentally hazardous materials contained in re-usable gaseous and liquid materials [2]. For instance, the removal of dye based toxic and carcinogenic pollutants from the industrial wastewater posing a severe hazard to aquatic living organisms [3, 4] has been of interest in numerous studies [5]. As thoroughly reviewed by Crain [6], ACs can be obtained from several different precursors such as agricultural-industrial solid wastes, natural materials, biosorbents and other miscellaneous sorbents through well-studied activation processes [7].

Use of agricultural waste products as AC precursor materials can be categorized as a renewable and low-cost alternative [8-13]. The choices of available natural materials, the activation routes and resulting adsorptive properties of ACs were recently reported in [14]. Considering the available data such as surface area, pore size and particle size, adsorption capacities of agricultural waste originated AC products are highly dependent on the natural precursor choice. Hence, the search for alternative natural precursors of ACs that are inexpensive, locally available and yet effective continues [14].

Sunflower (Helianthus annuus L.) is commonly planted and harvested for vegetable oil production from its seeds and some non-oil based products such as confectionary, horticulture, silage, etc. A recent USDA report [15] revealed that the global sunflower production of 45.65 million metric tons is shared by Ukraine (14m), Russia (11m), EU (8.6m), Argentina (3.4m), China (2.85m), Turkey (1.45m), US (1.2m) and other countries (3.15 m). Dominant industrial usage of sunflower is in oil production (from the seeds), food industry and more recently as a renewable energy source through biodiesel production [16]. In the production and harvesting cycle, sunflower stalks are commonly considered as high-volume waste materials as their conversion to specific added value products seems to be lacking. Furthermore, the research efforts towards the valorization of sunflower stalks are considerably limited [17-23].

Sunflower stalk is formed of two mechanically separable phases such as external fiber (90 % of dry weight) and internal pith, SP (10% of dry weight) [24]. Although the weight fraction of SP is relatively low, it covers most of the volume of the stalk due to its low density (0.035 g/cm^3) [25]. According to the Marecal et al. SP contains 3.2 % lignin, 4.4 % alkali extracted polysaccharides, 17.6% pectin, 45.4 % cellulose and 16.6 % ash [25]. During conventional pyrolysis conditions, decomposition of the organic fragments start with the decomposition of the pectin and polysaccharides, followed by cellulose decomposition, and finished with the lignin decomposition. Decomposition of organic fragments mostly pectin, cellulose and lignin fragments lead to the formation volatile products and at moderate heating rates and increase residence time of the volatiles, vapor phase components continue to react with each other as solid char is being formed. Aburto et al. showed that pectin pyrolysis start with initial depolymerization below 210 ^{o}C and pectin secondary decomposition continued until 580 ^{o}C resulted in residual char due to the chemical recombination of volatile products [26]. According to the Mohan et. al., hemicellulose fragments were produce less char yield than cellulose fragments and lignin decomposition produce

much more residual char that cellulose [27]. Independent from its chemical composition, the microstructure of SP is also unique providing its low density [25]. Therefore, this work aims to demonstrate production of AC from SP and demonstrate that SP porous structure increases the activation efficiency by offering potential activation sites that can result in high surface area ACs through alkaline hydroxide activation. In order to observe porous nature of the raw SP, computed tomography (CT) scan analysis was performed. Effects of carbonization and activation forming the SPAC were investigated by SEM, Raman and FTIR spectroscopy. Texture analysis was performed to discuss the result of activation process on the porous structure of ACs. In order to assess the adsorbative capability of the sunflower pith based AC in removing hazardous materials from water; adsorption isotherms and kinetics of methylene blue (MB) were studied as a model system.

2. Experimental

2.1. Sun Flower Pith Raw Material

Waste sunflower stalks were directly collected from a Düğüncülü agricultural area in Kırklareli, Turkey (one of the most prominent sunflower harvesting area in Turkey). Spongy pith material (Fig. 1) was extracted mechanically from the stalk and dried at 80^{o}C. Prior to carbonization process, the sunflower piths were ground and meshed so that the SP particles in size of 1mm or less were collected.

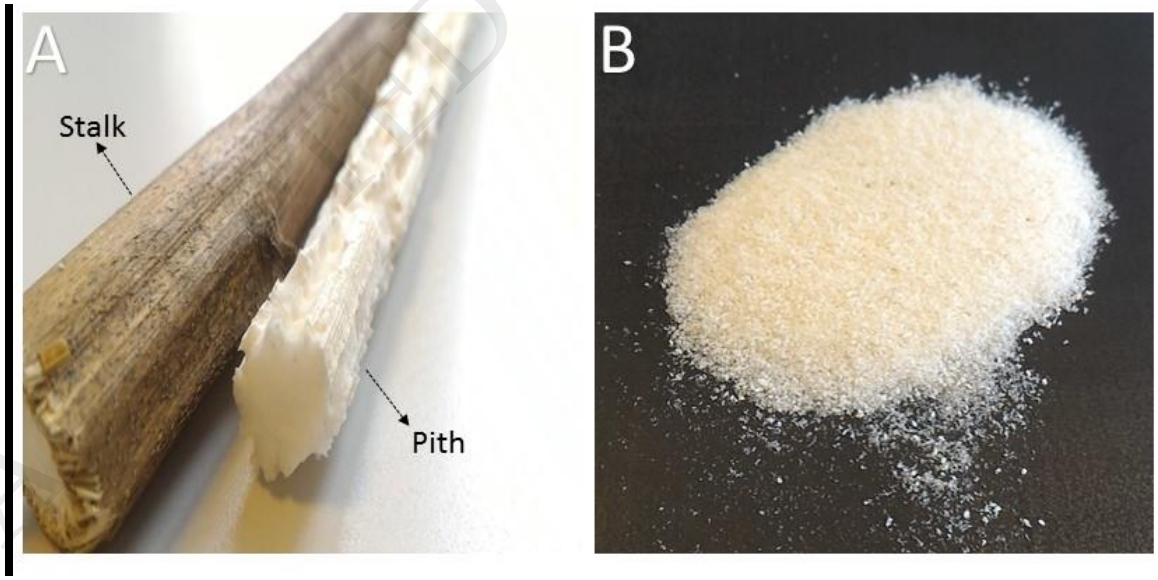

Fig. 1. a) Sunflower stalk and pith b) Powder form of SP.

2.2. Preparation of SP char

Raw sunflower pith particles were carbonized by conventional pyrolysis method with a heating rate of 10 ^{o}C/min [27, 28]. The maximum temperature for carbonization was adjusted to 500 ^{o}C for 2 hours under argon flow with a rate of 0.5 L/min. Then carbonization yield was calculated.

2.3. Preparation of activated carbon

Collected sunflower pith char (SPC) was chemically activated by two activating agents sodium hydroxide NaOH (purchased from Merck, Germany) and potassium hydroxide KOH (purchased from Merck, Germany) [28, 29]. First, 1-1.5 grams of SPC was mixed with the agent in a beaker with 20 ml distilled water. For all experiments, SPC/Base weight ratio was fixed to 1:3. Slurries were stirred for 1 hour to homogenize the mixture and then heated in an oil bath to the dryness. The dry powder mix was then ground in the mortar quickly to minimize exposure to moisture and loaded in a combustion boat. Activation was carried out at 700 ^{o}C for 1 hour (10 ^{o}C/min heating rate) in argon gas ambient for which the gas flow rate was 0.5 L/min. After the activation heating cycle was completed, the sample was cooled down at argon, and then washed with 0.1 M HCl (purchased from Merck, Germany) followed by hot water rinsing until the filtrate became neutral to make sure the activated agent residues and mineral matters were eliminated. Produced sunflower pith based activated carbon (SPAC) were finally dried at 80 ^{o}C under vacuum for 24 hours and kept sealed in a desiccator for further analyses.

2.4. Characterization of Sunflower Pith and its processed forms as char and active carbon particles

FTIR spectra of the raw sunflower pith (SP), its char (SPC), and activated carbon form (SPAC) were recorded over the range of 4000-550 cm^{-1} on a Thermo Scientific Nicolet iS10 spectrometer employing ATR apparatus. The total number of scans was 32 with a spectral resolution of 4 cm^{-1}. The assignment of the bands in the infrared spectra was in accordance with Shevla [30] and Baysal at al. [31].

Renishaw in Via Reflex Raman Microscope and Spectrometer was used for Raman scattering measurement at room temperature. Raman spectral analyses using visible excitation at 532 nm were done with a Nd-YAG laser power of 10 mW with data acquisition time of 10 s. The spectral range was selected as 800 cm^{-1} and 1800 cm^{-1}. Wire 3.1 software was used to fit adjusted peaks. Through the spectra, a linear baseline correction was applied.

The raw sunflower pith (SP) specimen before grinding was scanned with Skyscan1172 (Bruker co.) high-resolution micro-computed tomography (µCT) equipment at Sabancı University Nanotechnology and Application Center. In this µCT system, X-rays are generated with an electron accelerating voltage of 37 kV with a tungsten reflection and a beam current of 234 mA. Two-dimensional projection images with a resolution of 14 microns were reconstructed with

NRecon (version: 1.6.9.4) software which uses modified Feldkamp's back-projection algorithm [32]. Reconstructed three-dimensional objects, containing grayscale values for each pixel, have been segmented (binarized) by using the peak-valley method and analyzed via CTAn (CT-Analyser, version: 1.14.4.1) program. In order to obtain quantitative morphology parameters such as porosity, the volume of interest is chosen by virtually trimming the scanned 3D specimen as a cylinder in CTAn. Sampled cylinder containing gray-scale pixels has been binarized. Binary images contain only black and white pixels. Porosity measurement is one of the morphometric post-processing analysis that is performed by CTAn on a selected volume of interest. Within white pixels, as known as the objects, CTAn identifies the pores as black pixels surrounded by the white pixels. There are two types of porosity definition within CTAn. First one is the bubbles, better known as closed pores, where the volume of black pixels fully surrounded by on all sides by the white voxels. The second one is connecting channels, better known as the open pores, where a volume of black pixels located inside a solid object and that has a connection to the boundary of the volume of interest. Both closed and open pore calculations can be performed on layer level (2D) or object level (3D) and explain the morphology of the object.

Microstructural analyses of the raw SP, SPC, and SPACs were carried out using LEO Supra VP35 field emission scanning electron microscope.

Surface characterizations of the sunflower pith based sodium hydroxide activated carbons (N-SPAC), and potassium hydroxide activated carbons (K-SPAC) were conducted by Quantachrome Nova 2200e surface area analyzer. Samples were outgassed at 110 ^{o}C for 6 hours before analysis. N_2 adsorption studies were performed at -196 ^{o}C. BET Surface areas were measured from N_2 adsorption isotherms, pore size distribution was determined by DFT method, and micropore volume was calculated by DR method. The total pore volume of the samples was found by the volume of liquid nitrogen corresponding to the amount adsorbed at a relative pressure of P/P0 = 0.99. Mesopore volume was determined from the differences between the total pore volume and micropore volume.

2.5. Methylene blue adsorption experiments

Adsorption experiments were performed by using methylene blue (MB) as an adsorbate (purchased from Merck, Germany). Batch experiments were prepared using a set of concentration range varying from 50 ppm to 1000 ppm of MB, all by diluting 2000 ppm stock solution. 25 ml of each MB solutions were mixed with 25 mg of N-SPAC and K-SPAC in 100 ml serum bottles. Then, bottles that contain a different initial concentration of MB and SPAC were placed in a shaker at 25 ^{o}C and agitated at 200 rpm. Three hours equilibrium time was used for adsorption experiments. All samples were filtrated through 0.2 micrometers syringe filters in order to separate supernatant solution from the SPAC particles. Remaining dye concentration in the supernatant solutions was then calculated using UV-Vis spectrometer measuring adsorption intensities at a

wavelength of 664 nm in comparison to a previously recorded calibration curve of MB at 664 nm. Equilibrium uptake q_e(mg/g) associated with N-SPAC was calculated by equation 1.

$$q_e = \frac{(C_0 - C_e)V}{W} \quad (1)$$

where C_0 (mg/l), C_e (mg/L), and W (g) are initial and equilibrium concentrations (in a specific volume of solution (V (L)), and mass of adsorbent used, respectively. For all initial concentrations, equilibrium uptakes were calculated and fitted to the Langmuir and Freundlich isotherm models.

Langmuir [33] and Freundlich [34] isotherm models are widely used for a single solute system for describing dye adsorption at solid-liquid interfaces. Langmuir isotherm model suggests that all adsorption sites are equivalent and limited by monolayer coverage. Nonlinear form of the Langmuir model is derived as;

$$q_e = \frac{Q_m K_a C_e}{1 + K_a C_e} \quad (2)$$

Langmuir model parameters such as monolayer adsorption capacity per gram adsorbent (Q_m (mg/g) and Langmuir constant (K_a (L/mg)) related to rate of adsorption, can be calculated by determining q_e and C_e.

On the other hand, Freundlich isotherm model considers that adsorption sites are heterogeneous and surface energies are changing with surface coverage. Nonlinear Freundlich isotherm model is expressed as the following equation;

$$q_e = K_F C_e^{\frac{1}{n}} \quad (3)$$

Where K_F and n are Freundlich constants and K_F(L/mg) is the adsorption coefficient which represent the amount of the dye adsorbed at unit concentration. Heterogeneity factor "n" is the representation of how favorable adsorption process is.

Note that the nonlinear forms of adsorption isotherm models were used due to better representation of the experiment results [35-38]. Numerous researchers showed that linearized form of adsorption models have disadvantages because the transformation of nonlinear isotherms into a linear form results in variation in error distribution [38]. Nonlinear isotherm model parameters were calculated using a fitting procedure implemented via Solver add-in module of Microsoft Excel program.

Methylene Blue adsorption kinetic experiments

Adsorption kinetic experiments were conducted similarly to the adsorption equilibrium experiments. For each experiment, 25 ml of known concentration of MB solutions (mg/L) was mixed with 25 mg N-SPAC and withdrawn at different time intervals. Adsorption amount at any time q_t (mg/L) was calculated by;

$$q_t = \frac{(C_0 - C_t)V}{W} \quad (4)$$

where C_t (mg/L) is the remaining dye concentration at time, t. Initial concentrations were set to 500 and 1000 mg/L and adsorption time was considered up to 180 minutes.

Pseudo first-order [39], pseudo-second order [40], Elovich [41] and intraparticle diffusion [42] kinetic models were applied to understand adsorption dynamics related to the time for MB, N-SPAC system. Adsorption related to the diffusion from the boundaries usually follow pseudo first order kinetics, which is defined as;

$$q_t = q_e[1 - e^{-K_1 t}] \quad (5)$$

On the other hand, pseudo second order kinetic model follow whole range of adsorption and is represented as;

$$q_t = \frac{K_2 {q_e}^2 t}{1+K_2 q_e t} \quad (6)$$

Where $K_1$and K_2 are the adsorption rate constant (1/min) for pseudo first and second order adsorption.

Elovich equation is one of the most useful rate equation based on the adsorption capacity which is expressed as follows;

$$q_t = \frac{1}{\beta}\ln(1 + \alpha\beta t) \quad (7)$$

where β is the desorption constant (mg/g) related to the extent of coverage and activation energy of chemisorption and α is the initial adsorption rate (mg/g/min)

Another applicable model to understand diffusion mechanism is the intraparticle diffusion model purposed by Webber and Moris [42]. Intraparticle diffusion rate K_{id}(1/min) and Intercept C can be determined by equation 8.

$$q_t = K_{id} t^{0.5} + C \quad (8)$$

The best model was identified by the nonlinear fitting using Solver add-in in Excel. Most suitable model to describe the system was chosen by comparing correlation coefficient (R^2) values.

For comparing the applicability of the kinetic models, normalized standard deviation of the models was calculated by Eq. 7;

$$\Delta q_e\ (\%) = 100\sqrt{\sum \frac{[(q_e,exp - q_e,cal)/q_e,exp]^2}{N-1}} \quad (9)$$

Where N is the number of data points, q_e, exp and q_e, cal are the experimental and calculated equilibrium adsorption capacity, respectively.

3. Results and Discussions

3.1. Structural characterization

Computed Tomography (CT) Scan analysis has been suggested as an effective tool to characterize porous network structures [43, 44]. The morphological CT analysis of SP (Fig. 2a-c) showed that it contains on average 56 percent pore at each layer of the selected volume of interest (Table 1). The porosity analysis was performed as 2D and 3D scans separately by CTAn. Results show that the most of the closed pores that are observed at 2D SP layers are not closed in 3D. While 2D analysis characterized 96 % of the total porosity as closed pores, 99% of the pores was found open in the 3D analysis suggesting that pores on two dimensional layers (Fig. 2c) are connected on the z direction (stalk growth direction). The formation of 3D open pores is attributed to the interlaminar spacing of SP flakes and stacking of 2D closed pores on an x-y plane through z-direction. This lamellar formation was further explored by SEM (Fig. 2d-e) where individual layers of SP flakes (Fig 2e) are layer by layer aligned in the Z direction.

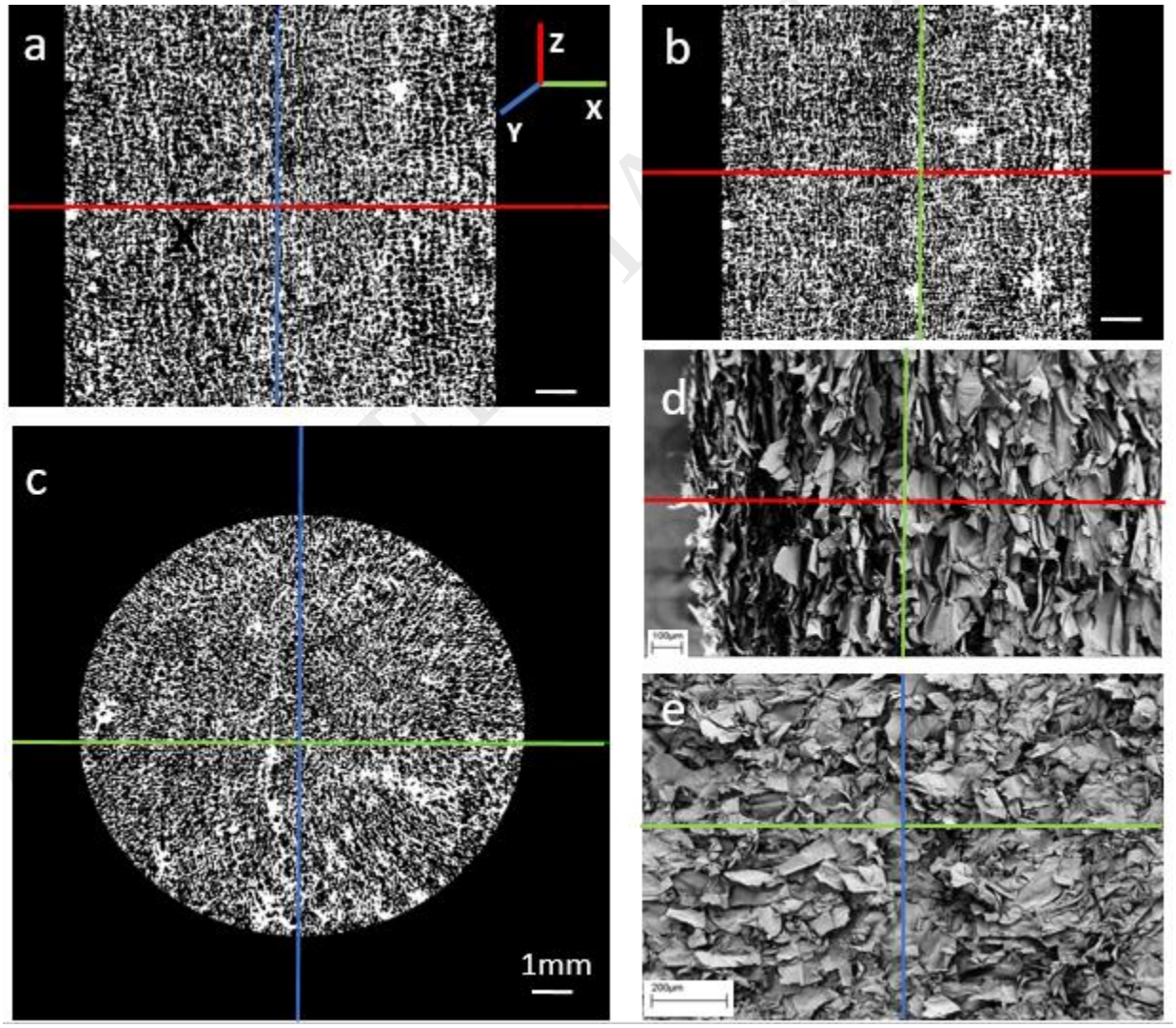

Fig. 2. (a) Raw SP CT scan on the z-y plane (b) Raw SP CT scan on the z-x plane (c) Raw SP CT scan on the x-y plane (d) SEM image of SP on the x-z plane e) SEM image of SP on the x-y plane.

Table 1
CT Scan porosity analysis of raw SP

Closed Porosity (%)		Open Porosity (%)		Total Porosity (%)	
2D Average	**3D**	**2D Average**	**3D**	**2D Average**	**3D**
53.58	0.02	4.28	57.53	55.57	57.54

SP is a soft, porous material, which has very high (70%) holocellulose content [21]. Most of the cellulosic parts of the pith were degraded during the pyrolysis. The yield of remaining char at 500 ^{o}C was around 35 %. After carbonization, stacked flakes in the raw structure were separated from each other. This might be the result of degradation of weak interactions between flat cells, which can easily break apart during pyrolysis [45]. On the other hand, it is very interesting that lamellar structure retained its form during carbonization. Individual SPC flakes after pyrolysis are shown in Fig. 3 (a-b). The in-plane widths of SPC flakes vary from 10 microns to 100 microns. Their thickness is around 200 nm with very little variation. Homogeneous distribution of the char flakes is a good indicator of the lamellar structure of the SPC and its derivative SPACs. It is a promising result for usage of SPCs in a high performance supercapacitor for electrode material [45, 46].

Chemical Activation of the SPC was conducted by alkaline hydroxides, NaOH and KOH. The Sunflower pith carbon (SPC) was impregnated with excess hydroxide solutions followed by a heat treatment. Chemical reactions of alkali-based activation follows the same mechanism as reported in the literature previously [41, 47, 48].
Activation yield was calculated according to the weight ratio of the raw SP to activated carbon SPAC. The activation agent NaOH resulted in 9-10% yield of N-SPAC, whereas the yield for K-SPAC (with KOH) was around 15%. Results show that NaOH activation provides a lower yield than KOH activation, due to the fact that NaOH is more reactive with lignocellulosic materials than KOH during activation. In Fig. 3(c-f), SEM analysis of the N-SPAC and K-SPAC, pore formation, and structure of the resulting activated carbons can be seen in detail. The figures suggest that a lamellar structure similar to the raw SP's inherent structure remained dominant despite harsh activation conditions with alkalines. The pore formation was further elaborated in textural analysis section 3.2

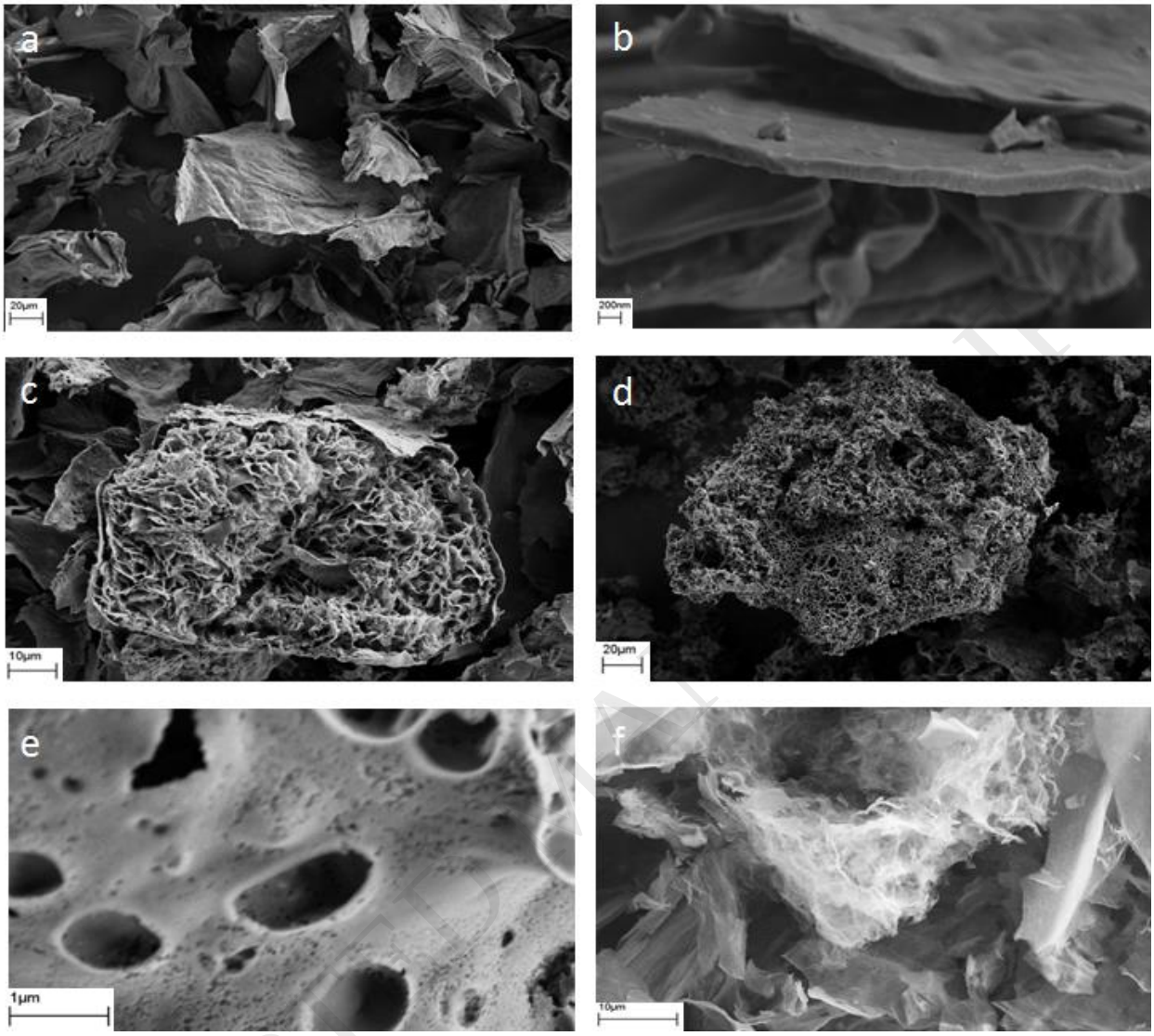

Fig. 3. (a) SPC structure (b) SPC flake thickness (c) N-SPAC (d) K-SPAC (e) Pore formation after activation (f) Lamellar structure after activation.

Raman spectroscopy gives information about microcrystalline carbon structure, such as the degree of ordering and crystallinity of carbon materials. Analysis of carbon crystalline structure by Raman spectroscopy, mostly focused on the investigation of G band (graphitic 1580 cm^{-1}), which represents crystalline graphite and D band (disorder 1360 cm^{-1}), that originates from various kinds of defects in graphitic structure [49]. The intensity ratio of the disordered carbon D band to the first order graphitic G band (I_D/I_G) in carbon structure is generally used to compare the degree of structural order and calculate in-plane crystallite size L_a [50, 51]. In this study, Raman spectroscopy was used to assess the degree of structural order of SPC and its derivatives Na-SPCA and K-SPCA to evaluate the effect of activation process on the microcrystalline structure. Raman spectrums obtained from SPC, N-SPAC, and K-SPAC exhibited two broad and overlapping peaks with intensity maxima located at around 1350 cm^{-1} (D-band) and 1590 cm^{-1} (G-band) (Fig. 4). Due

to the small crystallite size of biomass char and activated samples, widths of these two bands were considerably large like most of the disordered carbon materials. Ratios of the D band to G band get lower with higher structural alignment. I_D/I_G ratios of the SPC, N-SPAC, and K-SPAC were calculated as 0.971, 0.932 and 0.934, respectively. For all the samples, I_D/I_G ratios are lower than 1. It is attributed as an indicator of the high structural order of carbon which derived from sunflower pith compared to the other lignocellulosic biomass chars. I_D/I_G ratio of the activated samples seems to be slightly lower than the char. One can say that carbon skeleton of the char remained mostly unchanged after the activation. Moreover, the position of the G-band was blue shifted (*7 cm^{-1}*) to 1591 cm^{-1} for activated samples with respect to the SPC. It could be the result of the higher activation temperature, which leads to a higher extent of graphitization. Similar results were observed for biomass char in the literature suggesting higher carbonization temperature caused the G-band to shifted higher wavenumbers [52].

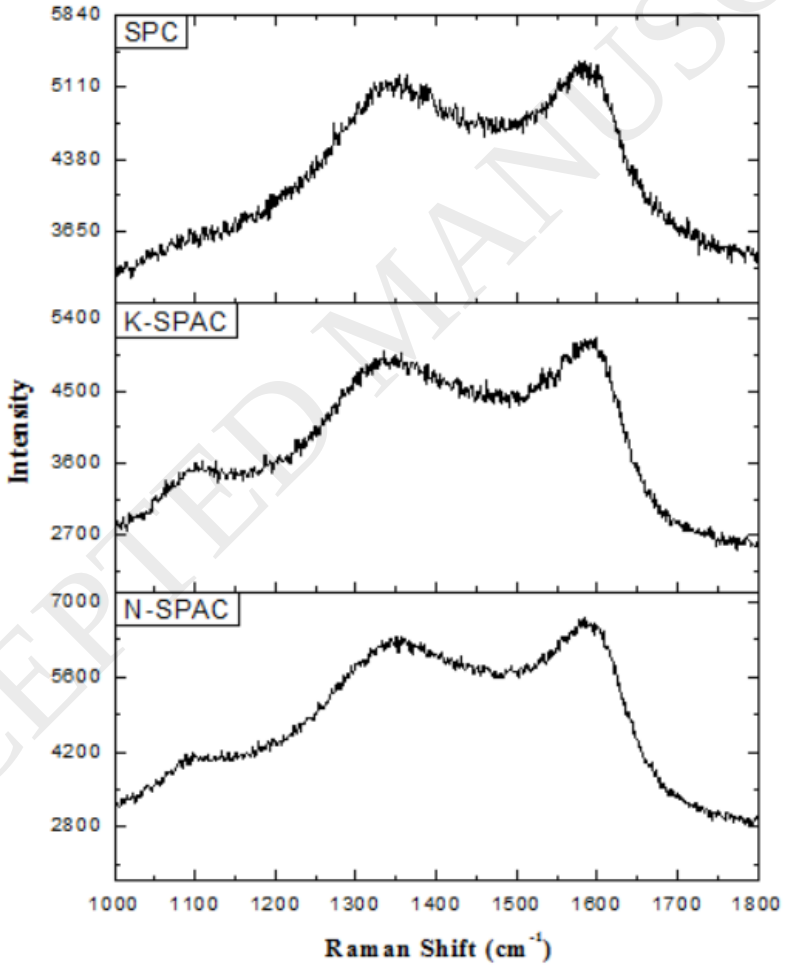

Fig. 4. Raman spectra of SPC and activated carbons.

FTIR analysis was utilized to evaluate the chemical structure of sunflower piths and functional group changes after carbonization and activation process. In Fig. 5, FTIR spectra of the raw

sunflower pith, SPA, and activated carbons SPAC were shown. The broadband near 3300 cm^{-1} in the FTIR spectra of raw SP is due to O–H and N-H groups. This band indicates that the organic matrix of the biomass has oxygen-containing functional groups and secondary bonding within the structure. Another distinct band around 2900 cm^{-1} represents C-H stretching vibration in the biomass. Peaks at 1730 cm^{-1} and broad adsorption band at 1600 cm^{-1} is related to the C=O stretching vibration of carbonyl groups (C=O), and C=C groups in the aromatic structure in the raw spectrum. The bands near 1420 cm^{-1} are due to the CH_2 asymmetric deformation, and aromatic C-C stretch [53] and bands between 1375 to 1100 cm^{-1} are assigned to phenol O-H bending [54], C-O stretching in carboxylic acids, alcohols and esters and phenolic C-O associated with lignin [41, 53, 54]. The broadband at 1050 cm−1 is associated with C-O-C stretching in cellulose and hemicellulose [54, 55]. Low-intensity bands were observed between 900-600 cm^{-1} regions due to the antisymmetric out-of-plane aromatic ring stretch [56] for the raw SP.

After carbonization, most of the functional groups in the raw SP diminish. The FTIR spectra of the SPC shows an apparent loss of functionalization in the region between 3500 to 1600 cm^{-1}, due to the loss of oxygen-containing groups and volatile aliphatic groups. The absence of the peak at 3250 cm^{-1} corresponds to a loss of the moisture and hydroxyl group during carbonization. Aliphatic C-H stretching around 2900 cm^{-1} also diminished due to complete removal of hydrogen containing aliphatic groups. Shoulder at 1578 cm^{-1} and peak at 1455 cm^{-1} are indications that the aromatic structure was still preserved after the carbonization although intensity decayed. The most intense peak in the SPC is at 1375 cm^{-1} and attributed to the phenolic C-O-H band. Important bands between 1300 to 1050 cm^{-1} represent C-O functional groups, mostly associated with the plant cellulose structure [57] in raw sample, lost their intensity after carbonization. This suggests that oxygen-containing groups related to the cellulose and hemicellulose fragments were decomposed during the carbonization at 500 ^{o}C, but phenolic groups, which are related to the lignin fragment of biomass were still present in the char derived from sunflower pith. FTIR spectra obtained from both N-SPAC and K-SPAC showed very similar trends.

Due to the carbonization and activation process, chemical bonds were broken, and most of the functional groups were loose. The intensities of the antisymmetric out-of-plane aromatic ring stretch between 900 to 600 cm^{-1} bands were observed very clearly because of the reduced total intensity of the spectrum as a result of the loss of functionality. The most distinct difference between char and activated compounds was the disappearance of 1375 cm-1 peak, related to the phenolic groups. It could be the result of decomposition of lignin part in the char during activation which was conducted at 700 ^{o}C.

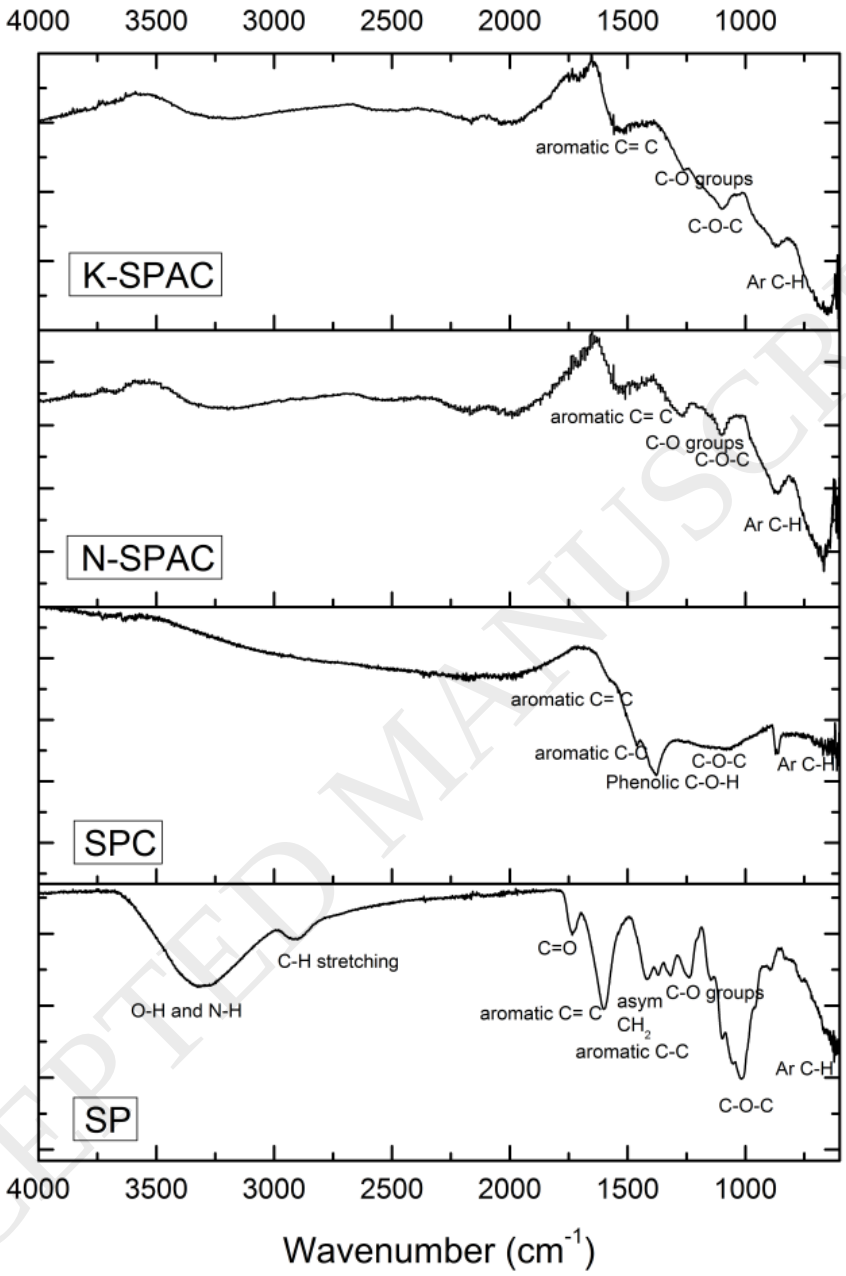

Fig. 5. FTIR spectra of Sunflower pith and its derivatives.

3.2. Textural characterization

Porous texture characterization of the activated carbon is an essential task to understand the effect of activation process and influence of the activating agent on SPC. For this reason, nitrogen adsorption and desorption isotherms at 77 K were determined to assess the porous structure of the

SPACs. N_2 adsorption isotherms of N-SPAC and K-SPAC are shown in Fig. 6(a), where shapes of the isotherms are an indicator of the porous texture of the activated carbons. The N_2 isotherms seemed like a combination of type I and type II isotherms according to the IUPAC classification due to the hysteresis loop between adsorption and desorption branches. Type I isotherm is associated with the monolayer adsorption representing high affinity between adsorbent and adsorbate which is a typical characteristic of micropore dominated materials. At low-pressure region, micropore filling is favorable which is followed by a mesopore filling contribution at high relative pressure region related to type II isotherm [41]. In N-SPAC adsorption isotherm, a steep increase over relative pressure of 0.1 was an indication of a wide range of micropore distribution. On the other hand, there was not any significant slope over the 0.1 P/P_0 range in K-SPAC isotherm, considered as an indication of more Langmuir type behavior. Microporosity distribution of this sample was narrower than N-SPAC. In addition, hysteresis loop between 0.3 - 0.8 relative pressure regions was associated with the capillary condensation in mesopores [58]. The shape of the hysteresis loop confirmed that narrow slit-like pores in both structures [58-60]. However, the hysteresis loop of the N-SPAC was wider and larger compared to the K-SPAC, which suggests that N-SPAC had a high ratio of mesopores and a wide range of mesopore development than K-SPAC [61]. The result of the isotherm analysis showed that pore development closely related to the activating agent [29]. According to isotherms, SPC activation with NaOH resulted in a high and wide range of porosity by combining micro and mesopores together. Whereas KOH activation of the SPC caused narrow pore size distribution with mostly micropore dominated.

Table 2

Porous texture characterization of N-SPAC and K-SPAC.

	SBET ($m^2\ g^{-1}$)	BET P/Po range	C constant	VT ($cm^3\ g^{-1}$)	Vu($cm^3\ g^{-1}$)	Vm ($cm^3\ g^{-1}$)	Vu/VT (%)	Dp (nm)
N-SPAC	2690	0.04 – 0.2	66	1.75	0.94	0.81	54	2.60
K-SPAC	2090	0.01 - 0.1	411	1.24	0.86	0.38	69	2.37

Porous texture analysis of the activated samples is shown in Table 2. BET surface areas of the samples were compatible with the isotherm analysis. The surface area of the NaOH activated N-SPAC was calculated as 2690 m^2/g, 29% higher than KOH activated K-SPAC surface area of 2090 m^2/g. A wide range of porosity increase was observed in N-SPAC surface area due to the combined effect of mesopores and micropores. BET equation is usually applied over the range from 0.05 to 0.3 relative pressures. However, it was observed that usual range was not applicable for K-SPAC sample. This is a general situation for microporous samples because of micropore filling is

completed at much lower relative pressures [58, 62]. This was another indication of the microporous texture of K-SPAC. Relative pressure ranges and calculated C constants for BET surface area determination were given in Table 2. The C constant calculated from BET equation is a qualitative result related to the enthalpy of monolayer adsorption. As it can be seen in Table 2, the C value of K-SPAC is higher than N-SPAC, an indication of the higher magnitude of adsorbent- adsorbate interaction energy common for micropore-dominated materials [58]. Total pore volumes of the N-SPAC and K-SPAC were calculated as 1.75 cm^3/g and 1.24 cm^3/g, respectively. The K-SPAC micropore volume was determined as 0.86 cm^3/g which cover 69 % of the total porosity. On the other hand, for N-SPAC, pore fractions were distributed by micro and mesopores. The N-SPAC micropore fraction was 54 % due to the higher mesopore development with NaOH activation compared to the KOH. The average pore diameter of N-SPAC and K-SPAC were calculated as 2.60 nm and 2.37 nm, respectively. The NaOH activated sample had wider pore development that resulted in higher average pore diameter. On the contrary, the KOH activated sample had lower average pore size due to the specific pore formation in micropore region. Pore developments of the activated samples can be observed in detail by pore size distributions as illustrated in Fig. 6(b). Both samples had a great number of pores accumulated in the micropore region, however, for the NaOH activated sample, a large volume of mesopore structures was determined between 2 nm to 5 nm. In addition, a wide range of mesopore distribution can be observed in the N-SPAC compared to the K-SPAC, which had also some mesopores very close to the micropore region around 2 nm. Textural analysis showed that KOH activation caused only micropore development with very narrow pore distribution which is responsible for the high surface area for K-SPAC. On the other hand, NaOH seemed to be more reactive with sunflower pith char which led micropores to merge and collapse in the structure forming the mesopores. The synergetic effect of the presence of mesopores and micropores in the structure can significantly enhance adsorption capacity of the N-SPAC, especially for large adsorbates such as dye molecules.

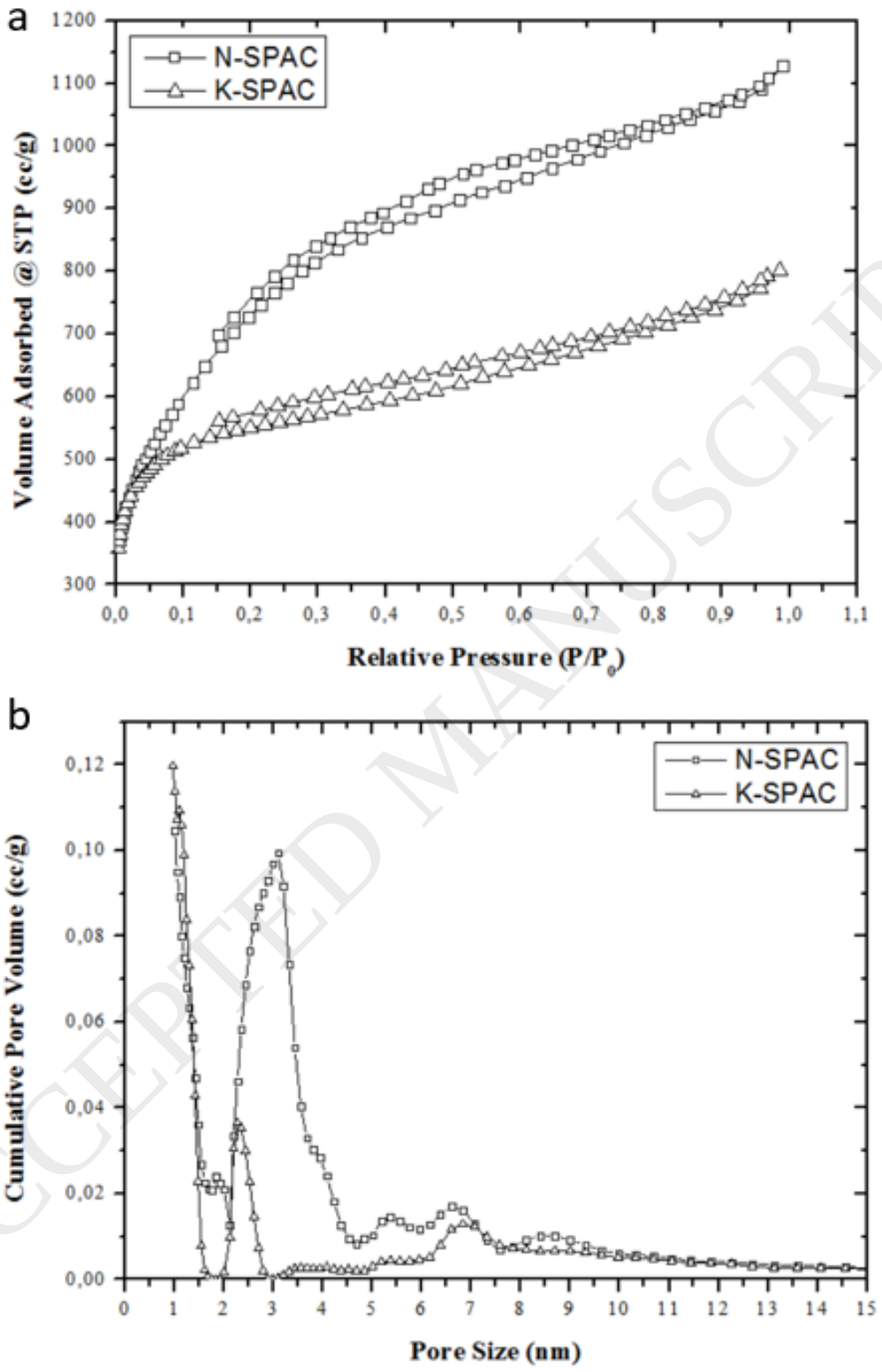

Fig. 6. (a) N_2 adsorption isotherms of N-SPAC and K-SPAC (b) NLDFT pore size disruption of N-SPAC and K-SPAC.

3.3. Adsorption and kinetic studies with methylene blue (MB)

N-SPAC was chosen for adsorption and kinetic studies with MB due to its higher surface area and a wide range of porosity that can lead to higher adsorption capacity and faster kinetics, even if a large dye molecule like MB was used as an adsorbate.

3.3.1. Adsorption Isotherms

Adsorption isotherms are very beneficial tools to predict adsorbent efficiency as they describe interactions between adsorbate molecules and adsorbent materials at equilibrium [63]. Therefore, analysis of the isotherm data as empirical equations is crucial for determining a suitable model that can be used for practical design and operation of the adsorbent systems [28]. In order to determine adsorption parameters, MB/N-SPAC and MB/K-SPAC systems were used as model systems. The width of MB molecule is 1.4 nm [28]; therefore, it can only enter large micropores bigger than its width [64]. It was shown that MB adsorption is not only related to the high surface area and pore volume and there is a significant contribution from mesopores [64, 65]. Langmuir and Freundlich isotherm models (Eq. 2 and 3, respectively) were used to analyze experimental data due to their wide usage of the describing dye adsorption at solid-liquid interfaces. Their nonlinear forms were fit to the experimental data as shown in Fig. 7.

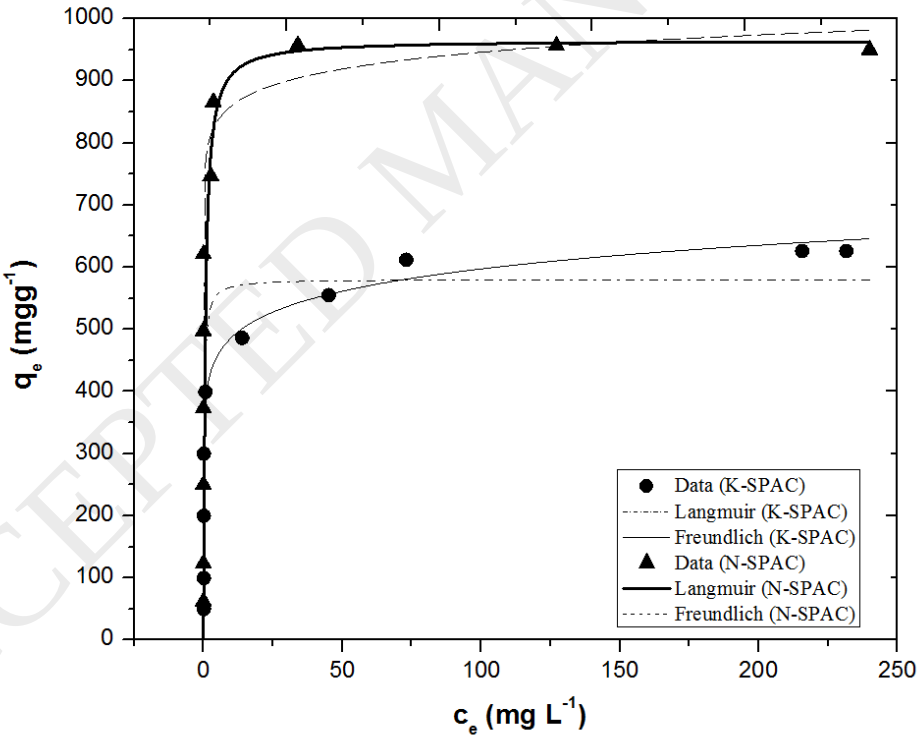

Fig. 7. Experimental data of MB/N-SPAC and MB/K-SPAC adsorption and nonlinear fitting of Langmuir and Freundlich models.

Table 3

Langmuir (Eq. 2) and Freundlich (Eq. 3) isotherm model parameters.

AC Type	Langmuir	Freundlich
N-SPAC	Q_m= 965.4 mg g^{-1} K_a= 1.612 L mg^{-1} R^2= 0.899	K_f = 780.5 mg g^{-1} η_f = 23.957 R^2= 0.701
K-SPAC	Q_m= 580.6 mg g^{-1} K_a= 4.553 L mg^{-1} R^2= 0.723	K_f = 396.19 mg g^{-1} η_f = 11.22 R^2= 0.912

Langmuir and Freundlich's model parameters are presented in Table 3. Langmuir monolayer adsorption capacity (Q_m) of the N-SPAC was equal to 965.349 mg/g. The coefficient of determination, R^2 value for the fit by Langmuir model was 0.899. On the other hand, the R^2 value for the Freundlich isotherm model based fit, which considers adsorption on the heterogeneous surface was 0.701. The heterogeneity factor nf is used to evaluate nature of the adsorption process. When adsorption is physical (nf > 1), linear (nf =1) or chemical (nf < 1). Calculated nf was greater than one that suggests physical nature of adsorption. Langmuir isotherm model's R^2 value was much higher than that of Freundlich model and calculated monolayer capacity is very close to the experimental adsorption capacity of N-SPAC, which is determined as 950 mg/g. According to the results, Langmuir adsorption model was a better fit for the experimental data leading to the conclusion that the surface is homogenous and adsorption of dye molecule occurred monolayer onto the N-SPAC surface.

When compared with. N-SPAC specimens, K-SPAC specimens had a significantly lower monolayer adsorption capacity (580.6 mg g^{-1}) Also adsorption mechanism rather followed Freundlich isotherm which suggested the presence of heterogenous adsorption sites. However, as reported above the yield of K-SPAC (%15) specimens is considerably higher than N-SPAC (%9-10) specimens which can make them economically more favorable.

Monolayer adsorption capacity of the N-SPAC is very high due to its high surface area, pore volume, and wide pore distribution. The mesopores and large micropores together allowed access of large dye molecules like MB into the whole surface of N-SPAC, i.e., high organic molecule uptake. Activated carbon prepared by sunflower pith facilitated one of the promising MB adsorption capacity compared to studies reported in the literature (Table 4).

Table 4

Maximum MB adsorption capacity of the various AC's derived from different agricultural waste based pre-cursors.

Adsorbate (AC source)	Acivation Technique	Specific Surface Area (m^2/g)	Q_{max} (mg/g)	Ref.
Sunflower Pith	NaOH	2690	965	This work
Sunflower Pith	KOH	2090	580.6	This work
Coconut Shell	NaOH	876.14	200	[66]
Coconut Shell	NaOH	2885	916.26	[28]
Coconut Shell	CO_2	1421	100	[67]
Coconut Shell	KOH/CO_2	1940	434.8	[68]
Coconut Shell	$ZNCl_2/CO_2$	1884	14.36	[69]
Tea	H_3PO_4	524	683.6	[70]
Banana Peel		1188	454.54	[71]
Grapefruit Peel		1198	456.28	
Mandarin Peel		1077	400	
Pomelo Peel		836	222.22	
Vetiver Roots	H_3PO_4	1004	423	[72]
	H_3PO_4+ Steam	1185	145	
Grape Waste	$ZNCl_2$	1455	417	[73]
Tomato Waste	$ZnCl_2$	1093	400	[74]
Coffee Grounds	H_3PO_4	925	367	[75]
Rattan Sawdust	KOH	1083	294.12	[76]
Buriti Shells	$ZnCl_2/CO_2$	843	275	[77]
P. oceanica (L.) dead leaves	$ZnCl_2$	1483	270.03	[78]
Oil Palm Shell	KOH	596.2	243.9	[79]
Cocoa Shell	CO_2	85	213	[80]
Cotton Stalk	$ZnCl_2$	794.84	315.45	[81]
Pine cone	$ZnCl_2$	939	60.97	[82]

3.3.2. Adsorption Kinetics

Determination of adsorption kinetics is important to understand the adsorption dynamics in terms of contact time and mass transfer of adsorbate. In order to find appropriate reaction order of the MB/N-SPAC system, experimental kinetic data were fit to a nonlinear form of pseudo first-order, pseudo second-order and Elovich kinetic models. Two different initial concentrations were chosen for adsorption kinetics experiments at low (500 mg/L) and high (1000 mg/L) adsorbate

concentration. Experimental data and model based curve fitting are shown in Fig. 8(a-b). At low initial concentration, adsorption kinetic was very fast and reached equilibrium in 10 minutes. Whereas at high initial concentration, adsorption kinetics was fast at the beginning, but it almost reached equilibrium in 3 hours.

At 500 mg/L initial concentration, pseudo first-order model and pseudo-second order reaction kinetic model coefficients of determination R^2 are 0.997 and 0.996, respectively (Table 4). They both had a low normalized standard deviation (Δq) from experimental data. However, the pseudo first-order model appeared more suitable with lowest Δq value, which was 2.26 %. This result signified that adsorption kinetics at low initial dye concentration is governed by adsorption process occurring on the adsorbent surface that based on the adsorbent capacity.

At 1000 mg/L initial concentration, neither pseudo first-order (R^2=0. 878, Δq = 17%) nor pseudo second-order model (R^2=0.936, Δq = 12%) fit well enough to the experimental data. However, the relatively high R^2 value of the pseudo second-order model was considered an indication of chemisorption related adsorption rate at high adsorbate concentration. The main reason for low correlation of pseudo second-order model was that chemisorption did not reach an endpoint even at high surface and bulk coverage after a long period of interaction time. On the other hand, Elovich model gave a considerably good fit to the experimental data. Its R^2 value (0.972) was higher, and Δq is about 7%. The Elovich model does not predict any definite mechanism but has been found useful in describing predominantly chemical adsorption on highly heterogeneous adsorbents [83]. Therefore, adsorption kinetics can be associated with chemisorption through the energetically heterogeneous active sites due to the wide pore structure of N-SPAC. Results suggested that at high initial MB concentrations, MB/N-SPAC adsorption process followed the Elovich model, which is related to the heterogeneous chemisorption mechanism.

However, relatively high Δq and low R^2 values due to the three kinetic models, at high initial adsorbate concentration chemisorption may not be stated as the sole rate determining step for MB adsorption kinetics on N-SPAC.

Table 5

Kinetic model parameters of MB/N-SPAC system at 500 mg/L and 1000 mg/L initial concentrations.

C_0 (mg L^{-1})	$Q_{e,exp}$ (mg g^{-1})	Pseudo First Order	Pseudo Second Order	Elovich	Intraparticle Diffusion
530	527.9	q_e =509.1 (mg g^{-1}) K_1= 0.4 (min^{-1}) R^2=0. 997 Δq= 2.3 %	q_e =517.7 (mg g^{-1}) K_2= 0.0026 (g mg^{-1} min^{-1}) R^2=0. 996 Δq= 2.7 %	α=509.5 (mg g^{-1} min^{-1}) β=0.01 (g mg^{-1}) R^2=0.810 Δq= 22.26%	K_{di1} = 64.6 (mg g^{-1} $min^{-1/2}$) C_1 = 297.7 (mg g^{-1}) K_{di2} =2.2 (mg g^{-1} $min^{-1/2}$) C_2 =489.2 (mg g^{-1}) R^2 = 0.692

1000	958.9	q_e =799.9 (mg g^{-1}) K_1= 0.2 (min^{-1}) R^2=0. 878 Δq= 17.0 %	q_e =875.4 (mg g^{-1}) K_2= 0.00022 (g g^{-1} min^{-1}) R^2=0. 936 Δq= 12.9 %	α= 1043.9 (mg g^{-1} min^{-1}) β=0.008 (g mg^{-1}) R^2=0.972 Δq= 6.6%	K_{di1} = 64.9 (mg g^{-1} $min^{-1/2}$) C_1 = 359.4 (mg g^{-1}) K_{di2} =40.0 (mg g^{-1} $min^{-1/2}$) C_2 =425.7 (mg g^{-1}) R^2 = 0.993

Another consideration in adsorption kinetics is intraparticle diffusion model suggested by Weber-Morris [42]. As the name implies, this model assumes that adsorption is related to the diffusion of the adsorbate molecules into the inner pores of adsorbent particles [84]. In Fig. 8 (c), Intraparticle diffusion plot of q_t versus $t^{1/2}$ can be seen. In case of a single straight line fitting the hole experimental data, adsorption is attributed only to the intraparticle diffusion. If the fitting requires two or more lines for representation of the data, it means that there are also other mechanisms that influence the adsorption other than the intraparticle diffusion. The plots of MB/N-SPAC system gave two straight lines for both concentrations. The line at early stages with higher slope indicated macro and mesopore filling and second line represents gradual adsorption into the micropores which are dominated by intraparticle diffusion [85, 86]. Both lines gave intercept, which showed that intraparticle diffusion was not the only rate limiting mechanism. Intraparticle diffusion parameters associated with the present data are listed in Table 4. K_{di1} and K_{di2} are the intraparticle diffusion constants for region 1 and region 2, respectively. C is the intercept which indicates the thickness of the boundary layer. For both concentrations, K_{di1} values were higher than K_{di2} values, which indicated that adsorption rates were higher in the first stages than the second stage. In the first stage, adsorption of MB onto the external surface (macro and mesopore structure) of N-SPAC caused high adsorption rates. On the other hand, in the second stage, the internal surface (micropore) filling was dominant, and the rate was getting slower which is governed by intraparticle diffusion. R^2 value of the 1000 mg/L initial concentration (0.993) is much higher than 500 mg/L initial MB concentration, which suggests that intraparticle diffusion was more favorable at high initial dye concentrations than at low dye concentrations. Kinetic results overall showed that for MB/N-SPAC systems, at 1000 mg/L initial MB concentration, intraparticle diffusion model played a significant role in the uptake of the adsorbate by N-SPAC.

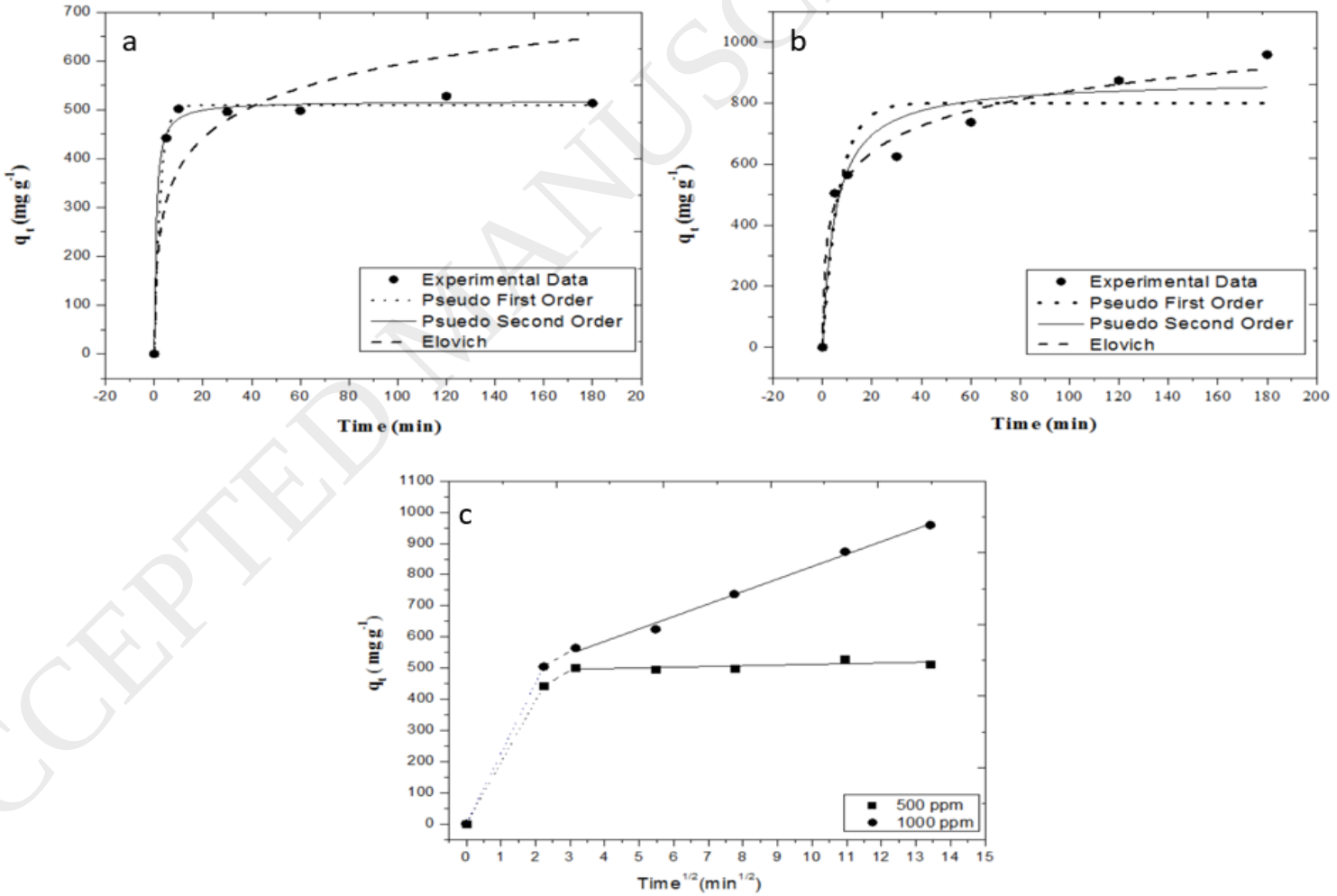

Fig. 8. (a) Non-linear fits by pseudo first-order, pseudo second-order and Elovich models at 500 mg/L initial MB concentration (b) Nonlinear fits by pseudo first-order, pseudo second-order and Elovich models at 1000 mg/L initial MB concentration (c) Intraparticle diffusion model plots of 500 and 1000 mg/L initial MB concentration.

4. Conclusion

The present study demonstrated that high surface area activated carbons can be prepared from waste-biomass sunflower piths by alkaline hydroxides. SEM analysis assisted by Micro CT of the raw sample showed lamellar network (flake-like structure) of the pith. Sunflower pith char (SPC) retained this flake-like form with a homogeneous distribution of flake thickness of around 200 nm. BET Surface area of the NaOH-activated N-SPAC was calculated as 2690 m^2/g that was higher than KOH-activated K-SPAC 2090 m^2/g. Textural analysis showed that the KOH activation caused mostly micropore development with very narrow pore distribution. On the other hand, NaOH seemed to be more reactive with the SPC, which resulted in micropores to merge and collapse in the structure to form also mesopores.

Maximum adsorption capacity of N-SPAC was calculated as 965mg/g whereas it was 580 mg/g for K-SPAC specimens.

Adsorption kinetic studies for N-SPAC revealed that at a low initial concentration of dye (500 mg/L), the pseudo first-order kinetic model was predictive. On the other hand, at high initial MB concentration (1000 mg/L), the results indicate that the adsorption kinetics follow the Elovich model with intraparticle diffusion as one of the rate-determining steps.

In summary, the N-SPAC prepared by SP had very high MB adsorption capacity due to its high surface area, pore volume, and wide pore size distribution. The combined effect of the mesopores and large micropores allowed access of large dye molecules like MB into the whole surface of the N-SPAC. On the other hand K-SPAC yield (%15) was higher than N-SPAC(%10) which can consolidate its usage from economic point of view in wastewater treatment technologies.

References

[1] H. Marsh, F. Rodríguez-Reinoso, CHAPTER 2 - Activated Carbon (Origins), Activated Carbon, Elsevier Science Ltd, Oxford, 2006, pp. 13-86.
[2] E. Forgacs, T. Cserháti, G. Oros, Removal of synthetic dyes from wastewaters: a review, Environment International 30 (2004) 953-971.
[3] C. O'Neill, F.R. Hawkes, D.L. Hawkes, N.D. Lourenço, H.M. Pinheiro, W. Delée, Colour in textile effluents – sources, measurement, discharge consents and simulation: a review, Journal of Chemical Technology & Biotechnology 74 (1999) 1009-1018.
[4] P.C. Vandevivere, R. Bianchi, W. Verstraete, Review: Treatment and reuse of wastewater from the textile wet-processing industry: Review of emerging technologies, Journal of Chemical Technology & Biotechnology 72 (1998) 289-302.
[5] G. Mezohegyi, F.P. van der Zee, J. Font, A. Fortuny, A. Fabregat, Towards advanced aqueous dye removal processes: A short review on the versatile role of activated carbon, Journal of Environmental Management 102 (2012) 148-164.
[6] G. Crini, Non-conventional low-cost adsorbents for dye removal: A review, Bioresource Technology 97 (2006) 1061-1085.
[7] S.J. Allen, L. Whitten, G. McKay, The Production and Characterisation of Activated Carbons: A Review, Developments in Chemical Engineering and Mineral Processing 6 (1998) 231-261.
[8] K.S. Bharathi, S.T. Ramesh, Removal of dyes using agricultural waste as low-cost adsorbents: a review, Applied Water Science 3 (2013) 773-790.
[9] K. Kadirvelu, M. Kavipriya, C. Karthika, M. Radhika, N. Vennilamani, S. Pattabhi, Utilization of various agricultural wastes for activated carbon preparation and application for the removal of dyes and metal ions from aqueous solutions, Bioresource Technology 87 (2003) 129-132.
[10] O. Ioannidou, A. Zabaniotou, Agricultural residues as precursors for activated carbon production—A review, Renewable and Sustainable Energy Reviews 11 (2007) 1966-2005.
[11] J.M. Dias, M.C.M. Alvim-Ferraz, M.F. Almeida, J. Rivera-Utrilla, M. Sánchez-Polo, Waste materials for activated carbon preparation and its use in aqueous-phase treatment: A review, Journal of Environmental Management 85 (2007) 833-846.
[12] D. Sud, G. Mahajan, M.P. Kaur, Agricultural waste material as potential adsorbent for sequestering heavy metal ions from aqueous solutions – A review, Bioresource Technology 99 (2008) 6017-6027.
[13] A. Demirbas, Agricultural based activated carbons for the removal of dyes from aqueous solutions: A review, Journal of Hazardous Materials 167 (2009) 1-9.
[14] A. Bhatnagar, W. Hogland, M. Marques, M. Sillanpää, An overview of the modification methods of activated carbon for its water treatment applications, Chemical Engineering Journal 219 (2013) 499-511.
[15] USDA, USDA report, https://www.sunflowernsa.com/stats/world-supply/, 2017.
[16] G. Antolín, F.V. Tinaut, Y. Briceño, V. Castaño, C. Pérez, A.I. Ramírez, Optimisation of biodiesel production by sunflower oil transesterification, Bioresource Technology 83 (2002) 111-114.
[17] S. Junyou, X. Yang, Study on the low cost and environmental cardboard made from pith of sunflower stalk, World Automation Congress 2012, 2012, pp. 1-4.
[18] L. Jiménez, F. López, Characterization of paper sheets from agricultural residues, Wood Science and Technology 27 (1993) 468-474.
[19] P. Vaithanomsat, S. Chuichulcherm, W. Apiwatanapiwat, Bioethanol production from enzymatically saccharified sunflower stalks using steam explosion as pretreatment, Proceedings of World Academy of Science, Engineering and Technology, 2009, pp. 140-143.
[20] M.J. Díaz, C. Cara, E. Ruiz, M. Pérez-Bonilla, E. Castro, Hydrothermal pre-treatment and enzymatic hydrolysis of sunflower stalks, Fuel 90 (2011) 3225-3229.

[21] G. Sun, X. Xu, Sunflower Stalks as Adsorbents for Color Removal from Textile Wastewater, Industrial & Engineering Chemistry Research 36 (1997) 808-812.
[22] A. Hashem, A. Abou-Okeil, A. El-Shafie, M. El-Sakhawy, Grafting of High α-Cellulose Pulp Extracted from Sunflower Stalks for Removal of Hg (II) from Aqueous Solution, Polymer-Plastics Technology and Engineering 45 (2006) 135-141.
[23] M. Jalali, F. Aboulghazi, Sunflower stalk, an agricultural waste, as an adsorbent for the removal of lead and cadmium from aqueous solutions, Journal of Material Cycles and Waste Management 15 (2013) 548-555.
[24] M. Xu, Polysaccharides from Sunflower Stalk Pith: Chemical, Structural, and Partial Physicochemical Characterization, 2016.
[25] V. Marechal, L. Rigal, Characterization of by-products of sunflower culture – commercial applications for stalks and heads, Industrial Crops and Products 10 (1999) 185-200.
[26] J. Aburto, M. Moran, A. Galano, E. Torres-García, Non-isothermal pyrolysis of pectin: A thermochemical and kinetic approach, Journal of Analytical and Applied Pyrolysis 112 (2015) 94-104.
[27] D. Mohan, C.U. Pittman, P.H. Steele, Pyrolysis of Wood/Biomass for Bio-oil: A Critical Review, Energy & Fuels 20 (2006) 848-889.
[28] A.L. Cazetta, A.M.M. Vargas, E.M. Nogami, M.H. Kunita, M.R. Guilherme, A.C. Martins, T.L. Silva, J.C.G. Moraes, V.C. Almeida, NaOH-activated carbon of high surface area produced from coconut shell: Kinetics and equilibrium studies from the methylene blue adsorption, Chemical Engineering Journal 174 (2011) 117-125.
[29] M.A. Lillo-Ródenas, J.P. Marco-Lozar, D. Cazorla-Amorós, A. Linares-Solano, Activated carbons prepared by pyrolysis of mixtures of carbon precursor/alkaline hydroxide, Journal of Analytical and Applied Pyrolysis 80 (2007) 166-174.
[30] C.L. Wilson, G. Svehla, Comprehensive analytical chemistry: Analytical infrated spectroscopy, Elsevier1976.
[31] M. Baysal, A. Yürüm, B. Yıldız, Y. Yürüm, Structure of some western Anatolia coals investigated by FTIR, Raman, 13C solid state NMR spectroscopy and X-ray diffraction, International Journal of Coal Geology 163 (2016) 166-176.
[32] M. Sugimori, F. Lam, Macro-void distribution analysis in strand-based wood composites using an X-ray computer tomography technique, Journal of Wood Science 45 (1999) 254-257.
[33] I. Langmuir, THE CONSTITUTION AND FUNDAMENTAL PROPERTIES OF SOLIDS AND LIQUIDS. PART I. SOLIDS, Journal of the American Chemical Society 38 (1916) 2221-2295.
[34] H.M.F. Freundlich, Uber die adsorption in losungen, Z. Phys. Chem. 57 (1906) 385-470.
[35] J. Vandenbruwane, S. De Neve, R.G. Qualls, S. Sleutel, G. Hofman, Comparison of different isotherm models for dissolved organic carbon (DOC) and nitrogen (DON) sorption to mineral soil, Geoderma 139 (2007) 144-153.
[36] J. He, S. Hong, L. Zhang, F. Gan, Y.-S. Ho, Equilibrium and thermodynamic parameters of adsorption of methylene blue onto rectorite, Fresenius Environmental Bulletin 19 (2010) 2651-2656.
[37] Z.L. Yaneva, B.K. Koumanova, N.V. Georgieva, Linear and Nonlinear Regression Methods for Equilibrium Modelling of p-Nitrophenol Biosorption by Rhizopus oryzae: Comparison of Error Analysis Criteria, Journal of Chemistry 2013 (2013) 10.
[38] S. Parimal, M. Prasad, U. Bhaskar, Prediction of Equillibrium Sorption Isotherm: Comparison of Linear and Nonlinear Methods, Industrial & Engineering Chemistry Research 49 (2010) 2882-2888.
[39] S.Y. Lagergren, Zur Theorie der sogenannten Adsorption gelöster Stoffe, 1898.
[40] Y.-S. Ho, Absorption of heavy metals from waste streams by peat, University of Birmingham, 1995.
[41] A.C. Martins, O. Pezoti, A.L. Cazetta, K.C. Bedin, D.A.S. Yamazaki, G.F.G. Bandoch, T. Asefa, J.V. Visentainer, V.C. Almeida, Removal of tetracycline by NaOH-activated carbon

produced from macadamia nut shells: Kinetic and equilibrium studies, Chemical Engineering Journal 260 (2015) 291-299.
[42] W. Weber, J. Morris, Advances in water pollution research, Proceedings of the First International Conference on Water Pollution Research, Pergamon Press Oxford, 1962, pp. 231.
[43] K. Jones, G. Ramakrishnan, M. Uchimiya, A. Orlov, New Applications of X-ray Tomography in Pyrolysis of Biomass: Biochar Imaging, Energy & Fuels 29 (2015) 1628-1634.
[44] L.Q.N. Tran, T.N. Minh, C.A. Fuentes, T.T. Chi, A.W. Van Vuure, I. Verpoest, Investigation of microstructure and tensile properties of porous natural coir fibre for use in composite materials, Industrial Crops and Products 65 (2015) 437-445.
[45] W. Qian, F. Sun, Y. Xu, L. Qiu, C. Liu, S. Wang, F. Yan, Human hair-derived carbon flakes for electrochemical supercapacitors, Energy & Environmental Science 7 (2014) 379-386.
[46] G. Hasegawa, K. Kanamori, T. Kiyomura, H. Kurata, T. Abe, K. Nakanishi, Hierarchically Porous Carbon Monoliths Comprising Ordered Mesoporous Nanorod Assemblies for High-Voltage Aqueous Supercapacitors, Chemistry of Materials 28 (2016) 3944-3950.
[47] M.A. Lillo-Ródenas, D. Cazorla-Amorós, A. Linares-Solano, Understanding chemical reactions between carbons and NaOH and KOH, Carbon 41 (2003) 267-275.
[48] E. Raymundo-Piñero, P. Azaïs, T. Cacciaguerra, D. Cazorla-Amorós, A. Linares-Solano, F. Béguin, KOH and NaOH activation mechanisms of multiwalled carbon nanotubes with different structural organisation, Carbon 43 (2005) 786-795.
[49] S. Potgieter-Vermaak, N. Maledi, N. Wagner, J.H.P. Van Heerden, R. Van Grieken, J.H. Potgieter, Raman spectroscopy for the analysis of coal: a review, Journal of Raman Spectroscopy 42 (2011) 123-129.
[50] F. Tuinstra, J.L. Koenig, Raman Spectrum of Graphite, The Journal of Chemical Physics 53 (1970) 1126-1130.
[51] D.S. Knight, W.B. White, Characterization of diamond films by Raman spectroscopy, Journal of Materials Research 4 (2011) 385-393.
[52] C. Guizani, K. Haddad, L. Limousy, M. Jeguirim, New insights on the structural evolution of biomass char upon pyrolysis as revealed by the Raman spectroscopy and elemental analysis, Carbon 119 (2017) 519-521.
[53] P.K. Adapa, C. Karunakaran, L.G. Tabil, G.J. Schoenau, Qualitative and Quantitative Analysis of Lignocellulosic Biomass using Infrared Spectroscopy, CSBE/SCGAB 2009 Annual ConferenceRodd's Brudenell River Resort, Prince Edward Island, 2009.
[54] K. Qian, A. Kumar, K. Patil, D. Bellmer, D. Wang, W. Yuan, R.L. Huhnke, Effects of biomass feedstocks and gasification conditions on the physiochemical properties of char, Energies 6 (2013) 3972-3986.
[55] C. Guizani, M. Jeguirim, S. Valin, L. Limousy, S. Salvador, Biomass Chars: The Effects of Pyrolysis Conditions on Their Morphology, Structure, Chemical Properties and Reactivity, Energies 10 (2017) 796.
[56] G. Várhegyi, P. Szabó, F. Till, B. Zelei, M.J. Antal, X. Dai, TG, TG-MS, and FTIR Characterization of High-Yield Biomass Charcoals, Energy & Fuels 12 (1998) 969-974.
[57] H.M. Al-Swaidan, A. Ahmad, Synthesis and characterization of activated carbon from Saudi Arabian dates tree's fronds wastes, 3rd International conference on chemical, biological and environmental engineering, 2011, pp. 25-31.
[58] Y.-C. Chiang, P.-C. Chiang, C.-P. Huang, Effects of pore structure and temperature on VOC adsorption on activated carbon, Carbon 39 (2001) 523-534.
[59] P.T. Williams, A.R. Reed, Development of activated carbon pore structure via physical and chemical activation of biomass fibre waste, Biomass and Bioenergy 30 (2006) 144-152.
[60] T. Zhang, W.P. Walawender, L.T. Fan, M. Fan, D. Daugaard, R.C. Brown, Preparation of activated carbon from forest and agricultural residues through CO2 activation, Chemical Engineering Journal 105 (2004) 53-59.

[61] N.R. Khalili, M. Campbell, G. Sandi, J. Golaś, Production of micro- and mesoporous activated carbon from paper mill sludge, Carbon 38 (2000) 1905-1915.
[62] K.S. Walton, R.Q. Snurr, Applicability of the BET Method for Determining Surface Areas of Microporous Metal−Organic Frameworks, Journal of the American Chemical Society 129 (2007) 8552-8556.
[63] R. Gong, J. Ye, W. Dai, X. Yan, J. Hu, X. Hu, S. Li, H. Huang, Adsorptive Removal of Methyl Orange and Methylene Blue from Aqueous Solution with Finger-Citron-Residue-Based Activated Carbon, Industrial & Engineering Chemistry Research 52 (2013) 14297-14303.
[64] S. Wang, Z.H. Zhu, A. Coomes, F. Haghseresht, G.Q. Lu, The physical and surface chemical characteristics of activated carbons and the adsorption of methylene blue from wastewater, Journal of Colloid and Interface Science 284 (2005) 440-446.
[65] C. Pelekani, V.L. Snoeyink, Competitive adsorption between atrazine and methylene blue on activated carbon: the importance of pore size distribution, Carbon 38 (2000) 1423-1436.
[66] M.A. Islam, M.J. Ahmed, W.A. Khanday, M. Asif, B.H. Hameed, Mesoporous activated coconut shell-derived hydrochar prepared via hydrothermal carbonization-NaOH activation for methylene blue adsorption, Journal of Environmental Management 203 (2017) 237-244.
[67] A. Jain, R. Balasubramanian, M.P. Srinivasan, Tuning hydrochar properties for enhanced mesopore development in activated carbon by hydrothermal carbonization, Microporous and Mesoporous Materials 203 (2015) 178-185.
[68] I.A.W. Tan, A.L. Ahmad, B.H. Hameed, Adsorption of basic dye on high-surface-area activated carbon prepared from coconut husk: Equilibrium, kinetic and thermodynamic studies, Journal of Hazardous Materials 154 (2008) 337-346.
[69] N. Kannan, M.M. Sundaram, Kinetics and mechanism of removal of methylene blue by adsorption on various carbons—a comparative study, Dyes and Pigments 51 (2001) 25-40.
[70] Y. Gokce, Z. Aktas, Nitric acid modification of activated carbon produced from waste tea and adsorption of methylene blue and phenol, Applied Surface Science 313 (2014) 352-359.
[71] P. Nowicki, J. Kazmierczak-Razna, R. Pietrzak, Physicochemical and adsorption properties of carbonaceous sorbents prepared by activation of tropical fruit skins with potassium carbonate, Materials & Design 90 (2016) 579-585.
[72] S. Altenor, B. Carene, E. Emmanuel, J. Lambert, J.-J. Ehrhardt, S. Gaspard, Adsorption studies of methylene blue and phenol onto vetiver roots activated carbon prepared by chemical activation, Journal of Hazardous Materials 165 (2009) 1029-1039.
[73] H. Sayğılı, F. Güzel, Y. Önal, Conversion of grape industrial processing waste to activated carbon sorbent and its performance in cationic and anionic dyes adsorption, Journal of Cleaner Production 93 (2015) 84-93.
[74] H. Sayğılı, F. Güzel, High surface area mesoporous activated carbon from tomato processing solid waste by zinc chloride activation: process optimization, characterization and dyes adsorption, Journal of Cleaner Production 113 (2016) 995-1004.
[75] A. Reffas, V. Bernardet, B. David, L. Reinert, M.B. Lehocine, M. Dubois, N. Batisse, L. Duclaux, Carbons prepared from coffee grounds by H3PO4 activation: Characterization and adsorption of methylene blue and Nylosan Red N-2RBL, Journal of Hazardous Materials 175 (2010) 779-788.
[76] B.H. Hameed, A.L. Ahmad, K.N.A. Latiff, Adsorption of basic dye (methylene blue) onto activated carbon prepared from rattan sawdust, Dyes and Pigments 75 (2007) 143-149.
[77] O. Pezoti, A.L. Cazetta, I.P.A.F. Souza, K.C. Bedin, A.C. Martins, T.L. Silva, V.C. Almeida, Adsorption studies of methylene blue onto ZnCl2-activated carbon produced from buriti shells (Mauritia flexuosa L.), Journal of Industrial and Engineering Chemistry 20 (2014) 4401-4407.
[78] M.U. Dural, L. Cavas, S.K. Papageorgiou, F.K. Katsaros, Methylene blue adsorption on activated carbon prepared from Posidonia oceanica (L.) dead leaves: Kinetics and equilibrium studies, Chemical Engineering Journal 168 (2011) 77-85.

[79] I.A.W. Tan, A.L. Ahmad, B.H. Hameed, Adsorption of basic dye using activated carbon prepared from oil palm shell: batch and fixed bed studies, Desalination 225 (2008) 13-28.
[80] F. Ahmad, W.M.A.W. Daud, M.A. Ahmad, R. Radzi, Cocoa (Theobroma cacao) shell-based activated carbon by CO2 activation in removing of Cationic dye from aqueous solution: Kinetics and equilibrium studies, Chemical Engineering Research and Design 90 (2012) 1480-1490.
[81] H. Deng, L. Yang, G. Tao, J. Dai, Preparation and characterization of activated carbon from cotton stalk by microwave assisted chemical activation—Application in methylene blue adsorption from aqueous solution, Journal of Hazardous Materials 166 (2009) 1514-1521.
[82] A. Özhan, Ö. Şahin, M.M. Küçük, C. Saka, Preparation and characterization of activated carbon from pine cone by microwave-induced ZnCl2 activation and its effects on the adsorption of methylene blue, Cellulose 21 (2014) 2457-2467.
[83] M.K. Aroua, S.P.P. Leong, L.Y. Teo, C.Y. Yin, W.M.A.W. Daud, Real-time determination of kinetics of adsorption of lead(II) onto palm shell-based activated carbon using ion selective electrode, Bioresource Technology 99 (2008) 5786-5792.
[84] M. Doğan, M. Alkan, A. Türkyilmaz, Y. Özdemir, Kinetics and mechanism of removal of methylene blue by adsorption onto perlite, Journal of Hazardous Materials 109 (2004) 141-148.
[85] V.C. Srivastava, M.M. Swamy, I.D. Mall, B. Prasad, I.M. Mishra, Adsorptive removal of phenol by bagasse fly ash and activated carbon: Equilibrium, kinetics and thermodynamics, Colloids and Surfaces A: Physicochemical and Engineering Aspects 272 (2006) 89-104.
[86] C. Valderrama, X. Gamisans, X. de las Heras, A. Farrán, J.L. Cortina, Sorption kinetics of polycyclic aromatic hydrocarbons removal using granular activated carbon: Intraparticle diffusion coefficients, Journal of Hazardous Materials 157 (2008) 386-396.